Measuring Valley Polarization in Two-Dimensional Materials with Second-Harmonic Spectroscopy

Yi Wei Ho, Henrique G. Rosa, Ivan Verzhbitskiy, Manuel J. L. F. Rodrigues, Takashi Taniguchi, Kenji Watanabe, Goki Eda, Vitor M. Pereira,* and José C. Viana-Gomes*

Read Online

ACCESS | Metrics & More | Article Recommendations | Supporting Information

ABSTRACT: A population imbalance at different valleys of an electronic system lowers its effective rotational symmetry. We introduce a technique to measure such imbalance (a valley polarization), which exploits the unique fingerprints of this symmetry reduction in the polarization-dependent second-harmonic generation (SHG). We present the principle and detection scheme in the context of hexagonal two-dimensional crystals, which include graphene-based systems and the family of transition metal dichalcogenides, and provide a direct experimental demonstration using a molybdenum diselenide monolayer with 2H polytype at room temperature. We deliberately use the simplest possible setup, where a single pulsed laser beam simultaneously controls the valley imbalance and tracks the SHG process. We further developed a model of the transient population dynamics, which analytically describes the valley-induced SHG rotation in very good agreement with the experimental data. In addition to providing the first experimental demonstration of the effect, this work establishes a conceptually simple, compact, and transferable way of measuring instantaneous valley polarization, with direct applicability in the nascent field of valleytronics.

KEYWORDS: *second-harmonic generation, valley polarization, transition metal dichalcogenides, graphene, 2D materials*
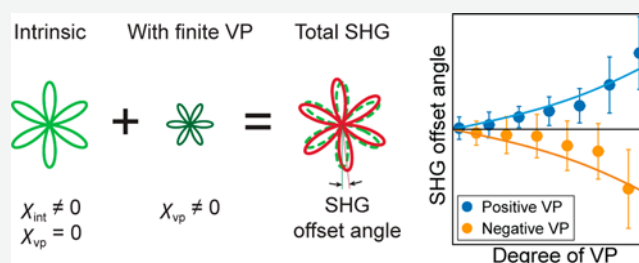
In semiconductors, "valleys" refer to local extrema of the electronic band structure in momentum space, that is, local maxima (minima) of the valence (conduction) band. Valleytronics aims to manipulate the population of charge carriers in each valley, which requires driving a population imbalance between nonequivalent valleys. The ability to induce, sustain, and control such a "valley polarization" (VP) endows electrons with a new (valley) degree-of-freedom to encode information,[1−3] beyond its charge and spin.

Systems based on graphene or transition metal dichalcogenides (TMDs) are forefront platforms to explore the promising field of valleytronics.[4] Their unique electronic structure features an underlying Diracness associated with two nonequivalent valleys ($\pm K$) enabled by the hexagonal crystal structure,[5] each valley carrying a finite Berry curvature.[4,6] This is compounded with their facile electrostatic (gate) tunability,[7] strong and rich interaction with light,[8] and the versatility offered by combining different monolayers in complex heterostructures.[9] Such features enabled the recent observation of valley Hall effect[10,11] or the optical excitation and quantum manipulation[12] of VP in this class of systems. Structures lacking inversion symmetry (e.g., monolayer TMDs or biased graphene multilayers), in particular, display an optical selection rule that allows remote control over the electronic population in each valley by shining either left (σ^+) or right (σ^-) circularly polarized light onto the sample.[9,13]

Crucial to support the development of valleytronics is the ability to detect and quantify the degree of VP on a sample with spatial resolution, instantaneously, and by noninvasive and expedite means. Up to now, this has been approached using polarization-resolved photoluminescence (PL)[14−17] and the magneto-optic Kerr effect[18−20]/circular dichroism.[21,22] However, VP detection by PL requires the material to have a bandgap, and the readout is convoluted with the excited state lifetime.[19,23] On the other hand, for the Kerr effect to arise, the material needs to have a strong spin−orbit coupling so that a VP correlates with circular dichroism.[11,19−22,24,25] Most significantly, both shortcomings impede their use in monolayer graphene, which has neither a gap nor a practically relevant spin−orbit coupling.[5]

Recent theoretical work proposed second-harmonic generation (SHG) to probe VP and valley-polarized currents in graphene and TMDs.[26−29] Governed by the second-order nonlinear susceptibility tensor $\chi^{(2)}$, SHG is an intrinsically robust feature of monolayer TMDs,[31−34] but is absent in
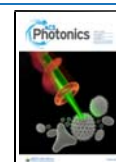
centrosymmetric crystals such as graphene or even-layered TMDs of the 2H polytype. In contrast, noncentrosymmetric crystals have finite $\chi^{(2)}$ components imposed by their point group symmetry. The point group of monolayer 2H-TMDs at equilibrium is D_{3h}, which implies that the nonzero components of the intrinsic $\chi^{(2)}$ are all related to a single quadratic susceptibility parameter:[35,36] $\chi_{\text{int}} \equiv \chi_{222}^{(2)} = -\chi_{211}^{(2)} = -\chi_{121}^{(2)} = -\chi_{112}^{(2)}$, where the Cartesian direction 2 is parallel to the crystal's vertical mirror symmetry. An out-of-equilibrium VP lowers this symmetry and gives rise to additional nonzero components,[28,29] namely, $\chi_{\text{vp}} \equiv \chi_{111}^{(2)} = -\chi_{122}^{(2)} = -\chi_{212}^{(2)} = -\chi_{221}^{(2)}$, where $\chi_{111}^{(2)} \neq \chi_{222}^{(2)}$. Consequently, the polarization-resolved SHG undergoes detectable changes according to the amount of VP induced.[28,29] For example, VP can be manifested by a chemical potential difference, $\Delta\mu$, between the valleys, and it can be shown that, to the lowest order, the magnitude of χ_{vp} increases linearly with $\Delta\mu$.[26,28,29,37] More generally, defining the degree of VP as $\Delta N \equiv N_+ - N_-$, where $N_\pm$ is the population at each of the $\pm K$ valleys, one expects $\chi_{\text{vp}} \propto \Delta N$ for a two-dimensional (constant density of states) system, whereas χ_{int} is independent of ΔN.

The contributions χ_{int} and χ_{vp} to the SHG may be distinguished by polarization spectroscopy because their respective second-order nonlinear polarizations, $\boldsymbol{P}^{(2)}$, point along orthogonal directions. Therefore, if the system has an intrinsic $\chi^{(2)}$, the emergence of VP is manifested by a rotation of the polarization-dependent SHG signal. More interestingly, in the case of graphene and other centrosymmetric crystals, where $\chi_{\text{int}} = 0$, gauging VP with SHG is even simpler, because the nonlinear effect can only arise from χ_{vp}; observation of SHG in such cases constitutes a direct detection of VP.

In this context, we report here the first experimental demonstration of SHG as an effective tool to probe VP at room temperature. In a home-built multiphoton microscope, a monolayer of molybdenum diselenide ($MoSe_2$) with 2H polytype is illuminated by a single laser beam that, if prepared with elliptical polarization (EP), can simultaneously induce VP and pump the SHG process. By continuously varying the beam's polarization state from linear to circular, we control the buildup of a valley imbalance which, correspondingly, causes the appearance and progressive development of a nonzero χ_{vp} contribution to $\chi^{(2)}$. This nonequilibrium component combines with the intrinsic second-order response and produces a well-defined rotation of the polarization-resolved SHG pattern.[34,38,39] The rotation directly yields the magnitude of χ_{vp}. As the same laser beam is used to both pump and probe (via SHG) the valley imbalance, this technique makes use of a simple setup that bypasses the need of superimposing two separate beams either in time or space.[18-22] It may thus be used to implement very compact, fast, and robust protocols to track the valley degree of freedom.

LINEARLY POLARIZED SHG

To best appreciate the nature of the effect and the underlying principle of operation, consider first the case where a valley-polarized $MoSe_2$ crystal is excited with linearly polarized light. With the electric field vector on the crystal plane, the nonlinear polarization vector is given by[28,29]

$$\begin{bmatrix} P_{ZZ}^{(2)} \\ P_{AC}^{(2)} \end{bmatrix} \propto \begin{bmatrix} \chi_{\text{vp}} & -\chi_{\text{vp}} & -\chi_{\text{int}} \\ -\chi_{\text{int}} & \chi_{\text{int}} & -\chi_{\text{vp}} \end{bmatrix} \begin{bmatrix} E_{ZZ}^2 \\ E_{AC}^2 \\ 2E_{ZZ}E_{AC} \end{bmatrix} \tag{1}$$

where E_{ZZ} and E_{AC} are the components of the incoming field along the zigzag (ZZ) and armchair (AC) directions, respectively. The existence of a nonequilibrium VP is reflected in the presence of the χ_{vp} terms that are otherwise absent in the intrinsic $\chi^{(2)}$ tensor at equilibrium. A simple inspection of eq 1 shows that the intensity of the SHG signal is independent of the incoming polarization angle, β, measured with respect to the AC direction. However, if the SHG signal is analyzed with a polarizer aligned in the same direction β as the pump field, the intensity becomes $S(\beta) \propto |\chi_{\text{int}} \cos 3\beta - \chi_{\text{vp}} \sin 3\beta|^2$, which explicitly depends on both the intrinsic and VP-induced contributions to $\chi^{(2)}$. One easily sees that the pattern described by $S(\beta)$ in a polar representation as a function of β corresponds to a scaling and rotation of the 6-fold pattern we obtain with $\chi_{\text{vp}} = 0$ (see Figure 1a). The rotation angle is $\Delta' \approx [\chi_{\text{vp}}/(3\chi_{\text{int}})] \cos \phi$, where ϕ is the relative phase between the complex χ_{int} and χ_{vp} (near a resonance, which is our case of interest, their phases are expected to be similar; thus, $\phi \approx 0$ and we consider $\{\chi_{\text{vp}}, \chi_{\text{int}}\} \in \mathbb{R}$, henceforth).
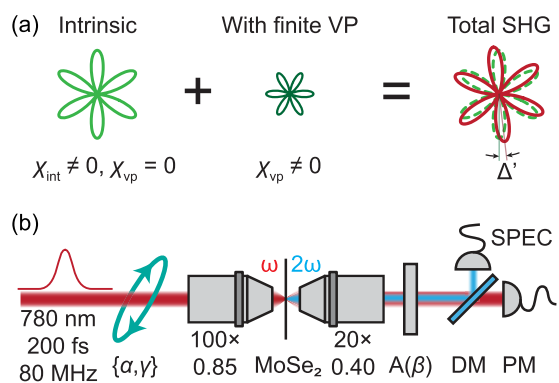

Figure 1. (a) Illustration of the combined effect of intrinsic and VP-induced $\chi^{(2)}$ components on the total SHG pattern after the linear analyzer. A finite VP translates in a rotation (Δ') of the SHG pattern relative to that of the crystal at equilibrium. (b) Experimental setup used to pump a $MoSe_2$ monolayer with an elliptically polarized pulsed laser beam (DM: dichroic mirror, PM: power meter, SPEC: spectrometer).

The readout method just discussed is illustrated in Figure 1a; it provides an intuitive way of measuring VP by tracking the rotation angle Δ'. The signal is characterized by a six-petal pattern and, other than the rotation and scaling induced by a finite VP, is analogous to the most commonly used SHG technique to find the lattice orientation of these crystals.[31,34,40,41] The key aspect is that, in the presence of a finite VP, the flower-shaped pattern rotates in relation to its orientation at equilibrium, with the amount of rotation directly related to the degree of VP. A simple variation of this protocol increases the rotation (hence, the sensitivity) by a factor of 3: Holding the incoming linear polarization along a fixed direction and rotating the analyzer by the relative angle β, the recorded SHG signal reads $S(\beta) \propto |\chi_{\text{int}} \cos \beta - \chi_{\text{vp}} \sin \beta|^2$. This yields a 2-fold pattern as a function of β (cf. Figure 2b), which rotates by the angle

$$\Delta = \tan^{-1}\left(\frac{\chi_{\text{vp}}}{\chi_{\text{int}}}\right) \approx \frac{\chi_{\text{vp}}}{\chi_{\text{int}}} \qquad (2)$$

with respect to its position in the absence of VP (the last result is valid if $|\chi_{\text{vp}}| \ll |\chi_{\text{int}}|$).
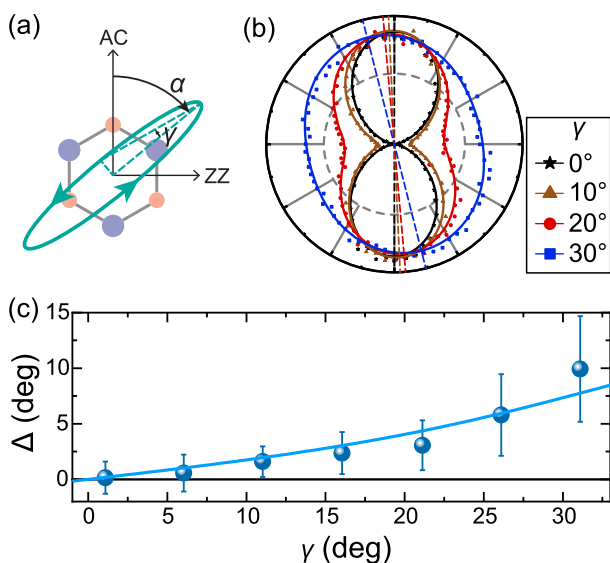

Figure 2. (a) Parameters α and γ that define the elliptical polarization state of the incoming light beam, and the orientation of the semimajor axis relative to the crystal lattice. (b) Representative measurements of the (normalized) SHG signal as a function of analyzer angle (the polar angle of the plot) for different helicities γ. Solid lines are the best fit to the experimental points. The dashed straight lines highlight the progressive rotation of the 2-fold pattern with increasing γ. (c) The rotation Δ of the SHG pattern as a function of helicity. In (b) and (c), the peak irradiance at the sample was 2.1 GW cm^{-2}.

We thus see that the presence of a VP can be optically detected and quantified in a rather simple SHG setup. By allowing that in a noninvasive and remote way, this approach can have many applications to directly monitor the valley degree of freedom in a number of valleytronics applications. While the previous discussion assumes that a VP has been established in the system by independent external means, we now show that the same simple setup can be used to probe the VP response of a crystal in equilibrium.

■ SIMULTANEOUS PUMPING AND PROBING VP

As we wish to demonstrate the rotation effect described above in a standalone crystal in equilibrium, we need a controllable way of inducing a population imbalance in the two valleys $\pm K$. This can be achieved by preparing the incoming beam in a state of elliptical polarization (EP), which we characterize by the helicity angle: $\sin 2\gamma = (I_+ - I_-)/(I_+ + I_-)$, where $I_\pm$ are the intensities of the two circular components in the beam. In a generic state with helicity $0 < |\gamma| < 45°$, the two intensities $I_\pm$ are different; since in MoSe$_2$ the σ^+ (σ^-) photons are selectively absorbed by particle-hole excitations only at the $+K$ ($-K$) valley,[14−17] EP light naturally induces different exciton populations at each valley by an amount that is controlled by the value of γ. At the same time, as long as $\gamma \neq \pm 45°$, an EP beam still drives SHG with the symmetries discussed above, and therefore, the rotation of the nonlinear signal can be tracked to monitor the VP in the system. This

allows one to simultaneously pump a VP on MoSe$_2$ and measure the magnitude of that VP, with the same laser beam.

A pulsed laser beam (Toptica FemtoFiber pro NIR, $\lambda = 780$ nm, $\hbar\omega = 1.59$ eV, $\tau = 200$ fs full-width at half-maximum pulse duration, 80 MHz repetition rate) was directed at a MoSe$_2$ monolayer according to the optical setup illustrated in Figure 1b. The photon energy is quasi-resonant with the lowest-lying exciton state ($\sim$19 meV above the PL peak at $E_A = 1.571$ eV, see Figure S1c in the Supporting Information). The monolayer was obtained by mechanical exfoliation from a 2H-MoSe$_2$ single-crystal, transferred to a fused silica substrate and encapsulated by 20 nm of hexagonal boron nitride to minimize environmental degradation. In addition to SHG spectroscopy, the single-layer character was validated by the Raman and PL spectroscopies (Supporting Information, section 1). All our optical measurements were performed under ambient conditions at room temperature. The incoming polarization was manipulated by a set of polarizers and waveplates. The semimajor axis of the polarization ellipse is oriented along α (see Figure 2a), which is kept constant and aligned to the AC direction of the sample, while γ is varied from $-30°$ to $+30°$. For each γ, the analyzer is rotated 360° to analyze the SHG signal before reaching a spectrometer. At the sample, the pump laser had an average power of few mW, focused by a 100× objective down to spot diameter of 1 μm.

A set of data for different values of γ is shown in the polar plots of Figure 2b. As expected for linearly polarized light ($\gamma = 0$), the analyzed SHG signal displays the pattern $S(\beta) \propto |\chi_{\text{int}}|^2 \cos^2 \beta$. A finite γ introduces two effects, which are evident in this figure: the minimum of the analyzed SHG signal is no longer at zero, and the 2-fold pattern undergoes a finite rotation that becomes more pronounced with increasing γ. While the first effect is a simple consequence of exciting the SHG with EP light,[28,29] the rotation is a fingerprint of VP due to the different rate at which σ^+ and σ^- photons are absorbed by the sample. Equation 2 shows that the amount of rotation Δ relative to the pattern for $\gamma = 0$ provides direct access to the nonequilibrium contribution (χ_{vp}) to $\chi^{(2)}$. The magnitude of χ_{vp}, in turn, provides a direct measure of the valley population imbalance.

A summary of the SHG rotation as a function of γ is shown in Figure 2c. At small γ, while the incoming polarization is still approximately linear, the population imbalance is small because $I_+ - I_- \ll I_+ + I_-$. Since, as pointed out earlier, in this regime, $\chi_{\text{vp}} \propto \Delta N$, one expects to see $\chi_{\text{vp}} \propto I_+ - I_- \propto \sin 2\gamma \approx 2\gamma$ and, according to eq 2, one anticipates $\Delta \propto \gamma$. The data reflects precisely this behavior and, as a result, confirms the predicted linear relation $\chi_{\text{vp}} \propto \Delta N$ at moderate valley pumping. To understand the full response curve at high γ in this single-beam setup we must consider the transient processes and partial saturation that takes place within each laser pulse, which we address below. Note that the error bars in Figure 2c grow with increasing γ because the SHG pattern becomes progressively more isotropic (cf. Figure 2b), which increases the error in the numerical fitting (Supporting Information, section 2) that is required to extract Δ.

Overall, these data establish two things: (i) that SHG is indeed an effective means of characterizing the degree of VP in the system and (ii) that a single-beam setup can be used, not only to probe, but also to simultaneously drive VP in a crystal from equilibrium. The latter aspect allows, for example, to characterize materials according to the valley population imbalance, ΔN, that is produced by a given helicity γ; this

response defines a material's "valley susceptibility" (see eq 5 for its detailed form).

TRANSIENT AND EFFECTIVE RESPONSE

Resolving the SHG pattern rotation with sufficient signal-to-noise ratio requires high irradiance, while, on the other hand, to efficiently pump VP (which is a linear optical absorption process), the absorption must not be saturated. As our experiment uses the same source to drive those two (first and second order) processes, it would seem to require a delicate compromise. The situation is facilitated by the use of an ultrafast pulsed laser beam (for which the recorded SHG signal is integrated over many pulses) and the fact that valley populations undergo complex transients within each pulse's duration (τ) due to various decay pathways on time scales comparable with τ.[42] To better understand these dynamics and how it defines the total SHG signal, we developed a model that considers the temporal evolution of the valley imbalance within one pulse and allows us to describe the SHG rotation in terms of the helicity γ at arbitrary power.

The quasi-resonance of the incoming photons with the A exciton, combined with the large exciton binding energy,[43] justifies modeling the key processes with a pair of two-level systems $\{|0\rangle, |\pm\rangle\}$, where $|0\rangle$ represents the ground state on either valley and $|\pm\rangle$ represents an A exciton belonging to the $\pm K$ valley. We consider the population rate equations,

$$\frac{dN_\pm}{dt} = -(\Gamma + \Gamma_{nr})N_\pm - \frac{\sigma(\omega)}{n\hbar\omega}I_\pm(N_\pm - N_{0,\pm}) - AN_\pm^2 \pm \Gamma_v(N_\mp - N_\pm)$$

(3)

where N_i represents the population in state $|i\rangle$, $\Gamma_{(nr)}$ is the (non) radiative recombination rate, A the exciton–exciton annihilation rate,[44] Γ_v the intervalley recombination rate, $I_\pm$ is the intensity of each circular component of the incoming light, $\sigma(\omega)$ is the MoSe$_2$ absorption cross-section, n is its refractive index, $\hbar\omega$ is the photon energy, and $N_\pm + N_{0,\pm} = N_T$ is the total density of available particle-hole excitations, which is an intrinsic property of MoSe$_2$ (details in Supporting Information, section 5). The laser pulse is modeled as $I(t) = I_0 f(t)$, where $f(t)$ is a Gaussian function characterized by the experimental width, τ. The last term in eq 3 describes intervalley exciton transitions which, in the specific case of MoSe$_2$, are known to contribute negligibly to the total exciton line width ($\Gamma_v \ll \Gamma + \Gamma_{nr}$), even at room temperature.[42] Moreover, in our experiment the photon detuning is only $\hbar\omega - E_A \simeq 19$ meV, below the 38 meV necessary to activate phonon-assisted intervalley relaxation.[17] Therefore, we set $\Gamma_v = 0$ (justified within the 200 fs width of the laser pulse) and solved the two eq 3 with the following parameters applicable to MoSe$_2$:[42,44,45] $\Gamma = 3.3$ ps^{-1}, $\Gamma_{nr} = 26.1$ ps^{-1}, $A = 0.33$ cm^2 s^{-1}, $\sigma(\omega) = N_T^{-1}(1 - \ln 0.06)$, where 0.06 is the absorption coefficient at 780 nm, and $N_T = 2.1 \times 10^{12}$ cm^{-2} (estimated from the laser line width and the electronic density of states; see Supporting Information, section 5.1).

Figure 3a shows the computed transient populations for different helicities γ of the incoming photons, as well as the imbalance $\Delta N(t) \equiv N_+(t) - N_-(t)$ (details in Supporting Information, section 5.2). [Note that setting $\Gamma_v = 0$ decouples the valleys and $\Delta N(t)$ is controlled only by $I_+(t) - I_-(t)$, which are also shown in the figure.] Even though these results were obtained with a peak pulse intensity (I_0) higher than the CW saturation (I_{sat}) by a factor of $I_0/I_{sat} \sim 10$ (see Supporting Information, Figure S10), no saturation of the transient
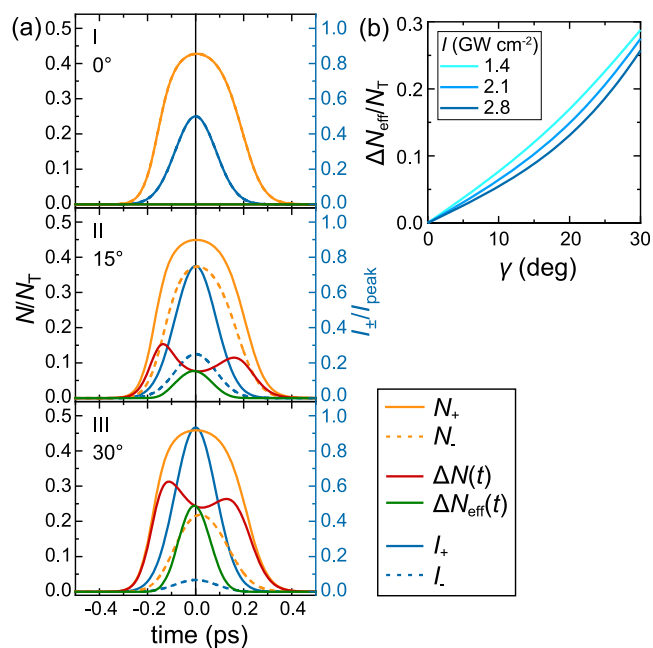

Figure 3. (a) Computed exciton populations at the $+K$ (N_+, solid orange curve) and $-K$ (N_-, dashed orange curve) valleys for $I_0 = 2.8$ GW cm^{-2} and $\gamma = 0°$ (I), 15° (II), and 30° (III). I_+ (solid blue curve) and I_- (dashed blue curve) are the σ^+ and σ^- intensity components of the laser pulse, respectively. The instantaneous population imbalance $\Delta N(t)$ is plotted in red while $\Delta N_{eff}(t) \equiv \Delta N(t)f^2(t)$ is shown in green. (b) Pulse-averaged population imbalance obtained with eq 4 as a function of γ and for a range of intensities covering those used in the experiments. It is an odd function of γ.

populations occurs since $N_\pm(t) < N_T/2$ at all times. With increasing helicity, a finite $\Delta N(t)$ is obtained throughout the whole pulse (red trace in panels II and III, Figure 3a). Its double-peak structure with a dip at the center arises because, with increasing γ, one of the populations (N_+) approaches the saturation limit ($N_\pm = N_T/2$) before the pulse reaches peak intensity; on that nonlinear regime, N_+ increases at a slower rate than N_-, which results in the central dip in $\Delta N(t)$. The key observation is that $\Delta N(t)$ remains finite throughout the entire pulse, even for the large irradiances required for SHG (see Figure S6c in the SI). It is, thus, appropriate to introduce a pulse-averaged population imbalance:

$$\Delta N_{eff} \equiv \frac{\int_{-\infty}^{\infty} \Delta N(t)f^2(t)dt}{\int_{-\infty}^{\infty} f^2(t)dt}$$

(4)

which defines the effective population imbalance that determines the amount of rotation in the SHG as recorded at the detector. In addition to deriving the above result, in Supporting Information, section 5.2, we show that ΔN_{eff} depends on the beam power and helicity according to

$$\frac{\Delta N_{eff}}{N_T} = \frac{bI_0/I_m \sin 2\gamma}{(bI_0/I_m + 1)^2 - (bI_0/I_m \sin 2\gamma)^2}$$

(5)

where $I_m = n\hbar\omega(\Gamma + \Gamma_{nr})/\sigma(\omega) = 7.6$ MW cm^{-2} and $b = 0.012$. With $b = 1$ this expression reduces to the steady state solution of eq 3 (Supporting Information, section 5.1). Despite the rich transient seen in Figure 3a, eq 5 shows that the dependence of the valley imbalance with laser power and helicity can still be captured by the steady state functional

dependence, but with a rescaled peak power: $I_0 \rightarrow bI_0$ (note that b is a parameter independent of I_0 and γ; see Supporting Information, section 5.2).

Equation 5 is plotted in Figure 3b and is seen to reproduce the experimental trend of Figure 2c. To make this more explicit and quantitative, we recall that, since $\chi_{vp} \propto \Delta N_{eff}$ we can write $\chi_{vp}/\chi_{int} = \kappa \, \Delta N_{eff}/N_T$ and combine eqs 2 and 5 to obtain the variation of Δ with γ (the constant κ can, in principle, be determined from a microscopic model of the optical response). Figure 4 shows the outcome of applying this procedure to fit the experimental rotation $\Delta(\gamma)$ at different laser power, with the constant κ as fitting parameter. We can see that this description captures the experimental behavior very well in Figure 4. The fit in Figure 4 yields $\kappa = 0.47 \pm 0.02$. This value means that if, for example, one induces a VP in the system of $\Delta N_{eff}/N_T = 10\%$, the valley-induced contribution to $\chi^{(2)}$ is expected to be $\chi_{vp}/\chi_{int} \approx 4.7\%$. [To emphasize the adequateness of our model in describing the experimental data in Figure 4, instead of fixing b to the value 0.012 obtained theoretically in Supporting Information, section 5.2, we can alternatively let both b and κ be free fitting parameters and simultaneously fit the experimental data in Figure 4a−c. Doing so yields $b = 0.012 \pm 0.003$ and, again, $\kappa = 0.47 \pm 0.04$, entirely in agreement with the theoretical result obtained for b.]
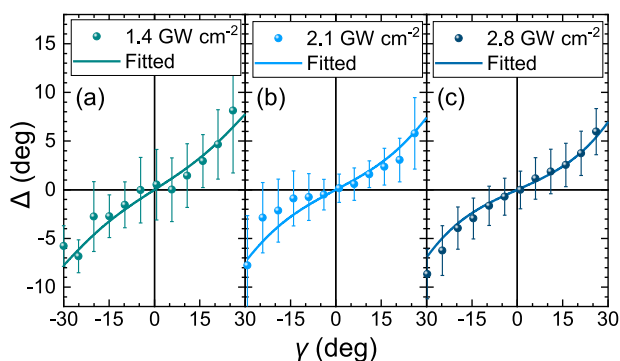

Figure 4. SHG rotation angle (Δ) against γ for different laser intensities. As discussed in the text, larger Δ indicates stronger VP. The solid lines are the best fit of each data set to eqs 2 and 5.

■ DISCUSSION AND CONCLUSIONS

Since SHG requires large irradiances (I_0), one could think that the observation of SHG rotation might be incompatible with efficient valley pumping and, thus, with a single-beam setup (for example, if I_0 is so large that absorption is saturated, the valley imbalance disappears). On the other hand, the results above show that a pulsed source allows a comfortable range of intensities where that compromise can be fulfilled. This is due to the ultrafast transient of the laser pulse and valley populations, which pushes the onset of saturation to values of I_0 much above I_{sat} under CW conditions[45] (see Supporting Information, Figure S10). We elaborate this in detail in Supporting Information, section 5.2 and Figures S7−S9. We show, in particular, the existence of an optimal intensity, I_{opt}, which provides the highest effective VP (highest ΔN_{eff}) at a given temperature ($I_{opt} \sim 1.3$ GW cm^{-2} at 300 K, Supporting Information, Figure S9). In terms of the plots shown in Figure 3, the value of I_{opt} corresponds to the threshold beyond which the central dip appears in the traces of $\Delta N(t)$; increasing I_0 past I_{opt} brings the magnitude of ΔN_{eff} down as the dip

intensifies. For this reason, the experimental intensities were chosen near the predicted I_{opt} for our material parameters (cf. Figure 4). Also important is, of course, the strong coupling of light to MoSe$_2$ (and 2D materials in general), which ensures a detectable nonlinear signal well before the onset of saturation.

It is important to stress, however, that this compromise is specific to using the same laser source for both optical processes, which is an extreme application of the principle of using SHG to quantify VP; this work establishes its applicability to such an extreme setting as well. In practice, no such constraint exists in all other scenarios where VP arises by other means (valley Hall effect, valley-polarized carrier injection, pumping from another laser, etc.). In such cases, we need only to track the SHG pattern; moreover, that can be done entirely with linearly polarized light, according to the much simpler protocol described earlier under "Linearly Polarized SHG".

One final remark relates to the Mott transition between the "exciton gas" and "electron-hole liquid" phases,[46] which occurs when the density of particle-hole pairs exceeds $\sim 1/a_X^2$ (a_X is the exciton radius) and which has been recently established theoretically and experimentally across the family of 2H TMDs.[47−52] At room temperature, the Mott transition is predicted[47−49] to occur at $\sim 10^{13}$ cm^{-2} in MoS$_2$, possibly higher in MoSe$_2$ on account of its larger binding energy[43] and consistent with recent measurements in MoSe$_2$/WSe$_2$ heterobilayers.[53] Although the peak power $\sim 1-3$ GW/cm^2 used in our experiment promotes high exciton densities, we seem to remain below the transition to the liquid phase given the agreement in Figure 4 between the observed and predicted behavior of the SHG rotation. (This is possibly aided by the small, but not insignificant, detuning from the excitonic resonance: $\hbar\omega - E_A = 19$ meV, while the pulse HWHM is ≈ 10 meV) At any rate, we stress that the fingerprint of nonzero VP in the SHG should remain even above the Mott threshold, simply because a valley imbalance always breaks the crystal's mirror symmetry, thereby inducing a finite χ_{vp}, irrespective of the nature of the excited populations. In fact, under asymmetric valley population, we expect correspondingly asymmetric redshifts of the exciton levels and bandgap near the Mott transition;[47,48] this should greatly reduce intervalley relaxation for lack of phase space, thus, sustaining VP for longer times and larger laser detuning.

In conclusion, we demonstrated that SHG spectroscopy can be a powerful tool for valleytronics, allowing to track and quantify the degree of VP. A single-beam SHG measurement allows simple protocols for remote characterization, including the ability to spatially map/scan nonuniform valley accumulation or diffusion, by analogy with the use of Kerr rotation spectroscopy in spintronics.[24] It could be especially suited to characterize the transport of valley currents in graphene, where recent experiments demonstrate the ability to inject spin-valley-polarized currents from adjacent TMDs at room temperature.[30,54] Moreover, as a parametric process, SHG is sensitive to the instantaneous degree of VP which, given the fast valley relaxation processes,[12] is an important advantage for operation at room temperature and photon energies with large detuning from the exciton levels, where other techniques such as PL stand at disadvantage.[19]

■ ASSOCIATED CONTENT

ⓢ Supporting Information

The Supporting Information is available free of charge at https://pubs.acs.org/doi/10.1021/acsphotonics.0c00174.

(1) Sample fabrication and characterization, (2) detailed data analysis, (3) conventional polarized second-harmonic generation, (4) nonlinear optical susceptibilities, (5) SH offset angle model, and (6) supplementary references (PDF)

■ AUTHOR INFORMATION

Corresponding Authors

Vitor M. Pereira − *Centre for Advanced 2D Materials and Department of Physics, National University of Singapore, Singapore 117546 Singapore*; Email: vpereira@nus.edu.sg

José C. Viana-Gomes − *Centre for Advanced 2D Materials and Department of Physics, National University of Singapore, Singapore 117546 Singapore; Center of Physics and Department of Physics, University of Minho, 4710-057 Braga, Portugal*; Email: phyvjc@nus.edu.sg

Authors

Yi Wei Ho − *NUS Graduate School for Integrative Sciences and Engineering, Singapore 119077 Singapore; Centre for Advanced 2D Materials and Department of Physics, National University of Singapore, Singapore 117546 Singapore;* ⓞ orcid.org/0000-0002-5487-4948

Henrique G. Rosa − *Centre for Advanced 2D Materials, National University of Singapore, Singapore 117546 Singapore;* ⓞ orcid.org/0000-0002-3184-9424

Ivan Verzhbitskiy − *Centre for Advanced 2D Materials and Department of Physics, National University of Singapore, Singapore 117546 Singapore;* ⓞ orcid.org/0000-0001-5945-8276

Manuel J. L. F. Rodrigues − *Centre for Advanced 2D Materials, National University of Singapore, Singapore 117546 Singapore; Center of Physics and Department of Physics, University of Minho, 4710-057 Braga, Portugal*

Takashi Taniguchi − *National Institute for Materials Science, Tsukuba 305-0044, Japan;* ⓞ orcid.org/0000-0002-1467-3105

Kenji Watanabe − *National Institute for Materials Science, Tsukuba 305-0044, Japan;* ⓞ orcid.org/0000-0003-3701-8119

Goki Eda − *Centre for Advanced 2D Materials, Department of Physics, and Department of Chemistry, National University of Singapore, Singapore 117546 Singapore;* ⓞ orcid.org/0000-0002-1575-8020

Complete contact information is available at:
https://pubs.acs.org/10.1021/acsphotonics.0c00174

Author Contributions

J.C.V. and V.M.P. conceived and supervised the experiments. Y.W.H., H.G.R., and M.J.L.F.R. performed the measurements. Y.W.H., J.C.V., and V.M.P. built the model. I.V. and G.E. fabricated the sample. T.T and K.W. provided BN crystals. Y.W.H., H.G.R., J.C.V., and V.M.P. wrote the paper. All authors discussed the results.

Notes

The authors declare no competing financial interest.

■ ACKNOWLEDGMENTS

■ REFERENCES

(1) Gunawan, O.; Shkolnikov, Y. P.; Vakili, K.; Gokmen, T.; De Poortere, E. P.; Shayegan, M. Valley Susceptibility of an Interacting Two-Dimensional Electron System. *Phys. Rev. Lett.* **2006**, *97* (18), 186404.

(2) Ang, Y. S.; Yang, S. A.; Zhang, C.; Ma, Z.; Ang, L. K. Valleytronics in Merging Dirac Cones: All-Electric-Controlled Valley Filter, Valve, and Universal Reversible Logic Gate. *Phys. Rev. B: Condens. Matter Mater. Phys.* **2017**, *96* (24), 245410.

(3) Rycerz, A.; Tworzydło, J.; Beenakker, C. W. J. J. Valley Filter and Valley Valve in Graphene. *Nat. Phys.* **2007**, *3* (3), 172−175.

(4) Schaibley, J. R.; Yu, H.; Clark, G.; Rivera, P.; Ross, J. S.; Seyler, K. L.; Yao, W.; Xu, X. Valleytronics in 2D Materials. *Nat. Rev. Mater.* **2016**, *1* (11), 16055 DOI: 10.1038/natrevmats.2016.55.

(5) Novoselov, K. S.; Geim, A. K.; Guinea, F.; Peres, N. M. R.; Castro Neto, A. H. The Electronic Properties of Graphene. *Rev. Mod. Phys.* **2009**, *81* (1), 109−162.

(6) Yu, H.; Cui, X.; Xu, X.; Yao, W. Valley Excitons in Two-Dimensional Semiconductors. *Natl. Sci. Rev.* **2015**, *2* (1), 57−70.

(7) Manzeli, S.; Ovchinnikov, D.; Pasquier, D.; Yazyev, O. V.; Kis, A. 2D Transition Metal Dichalcogenides. *Nat. Rev. Mater.* **2017**, *2*, 17033 DOI: 10.1038/natrevmats.2017.33.

(8) Mak, K. F.; Shan, J. Photonics and Optoelectronics of 2D Semiconductor Transition Metal Dichalcogenides. *Nat. Photonics* **2016**, *10* (4), 216−226.

(9) Xu, X.; Yao, W.; Xiao, D.; Heinz, T. F. Spin and Pseudospins in Layered Transition Metal Dichalcogenides. *Nat. Phys.* **2014**, *10* (5), 343−350.

(10) Mak, K. F.; McGill, K. L.; Park, J.; McEuen, P. L. The Valley Hall Effect in MoS2 Transistors. *Science* **2014**, *344* (6191), 1489−1492.

(11) Lee, J.; Mak, K. F.; Shan, J. Electrical Control of the Valley Hall Effect in Bilayer MoS_2 Transistors. *Nat. Nanotechnol.* **2016**, *11* (5), 421−425.

(12) Mak, K. F.; Xiao, D.; Shan, J. Light−Valley Interactions in 2D Semiconductors. *Nat. Photonics* **2018**, *12* (8), 451−460.

(13) Yao, W.; Xiao, D.; Niu, Q. Valley-Dependent Optoelectronics from Inversion Symmetry Breaking. *Phys. Rev. B: Condens. Matter Mater. Phys.* **2008**, *77* (23), 235406.

(14) Cao, T.; Wang, G.; Han, W.; Ye, H.; Zhu, C.; Shi, J.; Niu, Q.; Tan, P.; Wang, E.; Liu, B.; et al. Valley-Selective Circular Dichroism of Monolayer Molybdenum Disulphide. *Nat. Commun.* **2012**, *3* (1), 887.

(15) Zeng, H.; Dai, J.; Yao, W.; Xiao, D.; Cui, X. Valley Polarization in MoS2 Monolayers by Optical Pumping. *Nat. Nanotechnol.* **2012**, *7* (8), 490−493.

(16) Mak, K. F.; He, K.; Shan, J.; Heinz, T. F. Control of Valley Polarization in Monolayer MoS2 by Optical Helicity. *Nat. Nanotechnol.* **2012**, *7* (8), 494−498.

(17) Kioseoglou, G.; Hanbicki, A. T.; Currie, M.; Friedman, A. L.; Jonker, B. T. Optical Polarization and Intervalley Scattering in Single Layers of MoS_2 and $MoSe_2$. *Sci. Rep.* **2016**, *6* (1), 25041.

(18) Zhu, C. R.; Zhang, K.; Glazov, M.; Urbaszek, B.; Amand, T.; Ji, Z. W.; Liu, B. L.; Marie, X. Exciton Valley Dynamics Probed by Kerr Rotation in WSe_2 Monolayers. *Phys. Rev. B: Condens. Matter Mater. Phys.* **2014**, *90* (16), 161302.

(19) Hsu, W.-T.; Chen, Y.-L.; Chen, C.-H.; Liu, P.-S.; Hou, T.-H.; Li, L.-J.; Chang, W.-H. Optically Initialized Robust Valley-Polarized Holes in Monolayer WSe_2. *Nat. Commun.* **2015**, *6* (1), 8963.

(20) Yan, T.; Yang, S.; Li, D.; Cui, X. Long Valley Relaxation Time of Free Carriers in Monolayer WSe_2. *Phys. Rev. B: Condens. Matter Mater. Phys.* **2017**, *95* (24), 241406.

(21) Wang, Q.; Ge, S.; Li, X.; Qiu, J.; Ji, Y.; Feng, J.; Sun, D. Valley Carrier Dynamics in Monolayer Molybdenum Disulfide from Helicity-Resolved Ultrafast Pump-Probe Spectroscopy. *ACS Nano* **2013**, *7* (12), 11087–11093.

(22) Mai, C.; Barrette, A.; Yu, Y.; Semenov, Y. G.; Kim, K. W.; Cao, L.; Gundogdu, K. Many-Body Effects in Valleytronics: Direct Measurement of Valley Lifetimes in Single-Layer MoS_2. *Nano Lett.* **2014**, *14* (1), 202–206.

(23) Wang, G.; Palleau, E.; Amand, T.; Tongay, S.; Marie, X.; Urbaszek, B. Polarization and Time-Resolved Photoluminescence Spectroscopy of Excitons in $MoSe_2$ Monolayers. *Appl. Phys. Lett.* **2015**, *106* (11), 112101.

(24) Kato, Y. K.; Myers, R. C.; Gossard, A. C.; Awschalom, D. D. Observation of the Spin Hall Effect in Semiconductors. *Science* **2004**, *306* (5703), 1910–1913.

(25) Jin, C.; Regan, E. C.; Wang, D.; Iqbal Bakti Utama, M.; Yang, C.; Cain, J.; Qin, Y.; Shen, Y.; Zheng, Z.; Watanabe, K. Identification of Spin, Valley and Moiré Quasi-Angular Momentum of Interlayer Excitons. *Nat. Phys.* **2019**, *15*, 1140–1144.

(26) Wehling, T. O.; Huber, A.; Lichtenstein, A. I.; Katsnelson, M. I. Probing of Valley Polarization in Graphene via Optical Second-Harmonic Generation. *Phys. Rev. B: Condens. Matter Mater. Phys.* **2015**, *91* (4), 041404.

(27) Cheng, J.; Huang, D.; Jiang, T.; Shan, Y.; Li, Y.; Wu, S.; Liu, W.-T. Chiral Selection Rules for Multi-Photon Processes in Two-Dimensional Honeycomb Materials. *Opt. Lett.* **2019**, *44* (9), 2141–2144.

(28) Hipolito, F.; Pereira, V. M. Second Harmonic Spectroscopy to Optically Detect Valley Polarization in 2D Materials. *2D Mater.* **2017**, *4* (2), 021027.

(29) Hipolito, F.; Pereira, V. M. Corrigendum: Second Harmonic Spectroscopy to Optically Detect Valley Polarization in 2D Materials (2017 2D Mater. 4 021027). *2D Mater.* **2017**, *4* (3), 039501.

(30) Luo, Y. K.; Xu, J.; Zhu, T.; Wu, G.; McCormick, E. J.; Zhan, W.; Neupane, M. R.; Kawakami, R. K. Opto-Valleytronic Spin Injection in Monolayer MoS_2/Few-Layer Graphene Hybrid Spin Valves. *Nano Lett.* **2017**, *17* (6), 3877–3883.

(31) Li, Y.; Rao, Y.; Mak, K. F.; You, Y.; Wang, S.; Dean, C. R.; Heinz, T. F. Probing Symmetry Properties of Few-Layer MoS_2 and h-BN by Optical Second-Harmonic Generation. *Nano Lett.* **2013**, *13* (7), 3329–3333.

(32) Kumar, N.; Najmaei, S.; Cui, Q.; Ceballos, F.; Ajayan, P. M.; Lou, J.; Zhao, H. Second Harmonic Microscopy of Monolayer MoS_2. *Phys. Rev. B: Condens. Matter Mater. Phys.* **2013**, *87* (16), 161403.

(33) Rosa, H. G.; Junpeng, L.; Gomes, L. C.; Rodrigues, M. J. L. F.; Haur, S. C.; Gomes, J. C. V. Second-Harmonic Spectroscopy for Defects Engineering Monitoring in Transition Metal Dichalcogenides. *Adv. Opt. Mater.* **2018**, *6* (5), 1701327.

(34) Rosa, H. G.; Ho, Y. W.; Verzhbitskiy, I.; Rodrigues, M. J. F. L.; Taniguchi, T.; Watanabe, K.; Eda, G.; Pereira, V. M.; Gomes, J. C. V. Characterization of the Second- and Third-Harmonic Optical Susceptibilities of Atomically Thin Tungsten Diselenide. *Sci. Rep.* **2018**, *8* (1), 10035.

(35) Shen, Y. R. *The Principles of Nonlinear Optics*; Wiley: Chichester; New York, 2003.

(36) Boyd, R. W. *Nonlinear Opt.*, 3rd ed.; Academic Press: Burlington, MA, 2008.

(37) Golub, L. E.; Tarasenko, S. A. Valley Polarization Induced Second Harmonic Generation in Graphene. *Phys. Rev. B: Condens. Matter Mater. Phys.* **2014**, *90* (20), 201402.

(38) Autere, A.; Jussila, H.; Dai, Y.; Wang, Y.; Lipsanen, H.; Sun, Z. Nonlinear Optics with 2D Layered Materials. *Adv. Mater.* **2018**, *30* (24), 1705963.

(39) Autere, A.; Jussila, H.; Marini, A.; Saavedra, J. R. M.; Dai, Y.; Säynätjoki, A.; Karvonen, L.; Yang, H.; Amirsolaimani, B.; Norwood, R. A.; et al. Optical Harmonic Generation in Monolayer Group-VI Transition Metal Dichalcogenides. *Phys. Rev. B: Condens. Matter Mater. Phys.* **2018**, *98* (11), 115426.

(40) Malard, L. M.; Alencar, T. V.; Barboza, A. P. M.; Mak, K. F.; de Paula, A. M. Observation of Intense Second Harmonic Generation from MoS_2 Atomic Crystals. *Phys. Rev. B: Condens. Matter Mater. Phys.* **2013**, *87* (20), 201401.

(41) Ribeiro-Soares, J.; Janisch, C.; Liu, Z.; Elías, A. L.; Dresselhaus, M. S.; Terrones, M.; Cançado, L. G.; Jorio, A. Second Harmonic Generation in WSe_2. *2D Mater.* **2015**, *2* (4), 045015.

(42) Selig, M.; Berghäuser, G.; Raja, A.; Nagler, P.; Schüller, C.; Heinz, T. F.; Korn, T.; Chernikov, A.; Malic, E.; Knorr, A. Excitonic Linewidth and Coherence Lifetime in Monolayer Transition Metal Dichalcogenides. *Nat. Commun.* **2016**, *7* (1), 13279.

(43) Wang, G.; Chernikov, A.; Glazov, M. M.; Heinz, T. F.; Marie, X.; Amand, T.; Urbaszek, B. Colloquium: Excitons in Atomically Thin Transition Metal Dichalcogenides. *Rev. Mod. Phys.* **2018**, *90* (2), 21001.

(44) Kumar, N.; Cui, Q.; Ceballos, F.; He, D.; Wang, Y.; Zhao, H. Exciton-Exciton Annihilation in $MoSe_2$ Monolayers. *Phys. Rev. B: Condens. Matter Mater. Phys.* **2014**, *89* (12), 125427.

(45) Nie, Z.; Trovatello, C.; Pogna, E. A. A.; Dal Conte, S.; Miranda, P. B.; Kelleher, E.; Zhu, C.; Turcu, I. C. E.; Xu, Y.; Liu, K.; et al. Broadband Nonlinear Optical Response of Monolayer $MoSe_2$ under Ultrafast Excitation. *Appl. Phys. Lett.* **2018**, *112* (3), 031108.

(46) Shah, J.; Combescot, M.; Dayem, A. H. Investigation of Exciton-Plasma Mott Transition in Si. *Phys. Rev. Lett.* **1977**, *38* (25), 1497–1500.

(47) Steinhoff, A.; Rösner, M.; Jahnke, F.; Wehling, T. O.; Gies, C. Influence of Excited Carriers on the Optical and Electronic Properties of MoS_2. *Nano Lett.* **2014**, *14* (7), 3743–3748.

(48) Meckbach, L.; Stroucken, T.; Koch, S. W. Giant Excitation Induced Bandgap Renormalization in TMDC Monolayers. *Appl. Phys. Lett.* **2018**, *112* (6), 061104.

(49) Rustagi, A.; Kemper, A. F. Theoretical Phase Diagram for the Room-Temperature Electron-Hole Liquid in Photoexcited Quasi-Two-Dimensional Monolayer MoS_2. *Nano Lett.* **2018**, *18* (1), 455–459.

(50) Chernikov, A.; Ruppert, C.; Hill, H. M.; Rigosi, A. F.; Heinz, T. F. Population Inversion and Giant Bandgap Renormalization in Atomically Thin WS_2 Layers. *Nat. Photonics* **2015**, *9* (7), 466–470.

(51) Yu, Y.; Bataller, A. W.; Younts, R.; Yu, Y.; Li, G.; Puretzky, A. A.; Geohegan, D. B.; Gundogdu, K.; Cao, L. Room-Temperature Electron−Hole Liquid in Monolayer MoS_2. *ACS Nano* **2019**, *13* (9), 10351–10358.

(52) Bataller, A. W.; Younts, R. A.; Rustagi, A.; Yu, Y.; Ardekani, H.; Kemper, A.; Cao, L.; Gundogdu, K. Dense Electron−Hole Plasma Formation and Ultralong Charge Lifetime in Monolayer MoS2 via Material Tuning. *Nano Lett.* **2019**, *19* (2), 1104–1111.

(53) Wang, J.; Ardelean, J.; Bai, Y.; Steinhoff, A.; Florian, M.; Jahnke, F.; Xu, X.; Kira, M.; Hone, J.; Zhu, X.-Y. Optical Generation of High Carrier Densities in 2D Semiconductor Heterobilayers. *Sci. Adv.* **2019**, *5* (9), No. eaax0145.

(54) Safeer, C. K.; Ingla-Aynés, J.; Herling, F.; Garcia, J. H.; Vila, M.; Ontoso, N.; Calvo, M. R.; Roche, S.; Hueso, L. E.; Casanova, F. Room-Temperature Spin Hall Effect in Graphene/MoS_2 van Der Waals Heterostructures. *Nano Lett.* **2019**, *19* (2), 1074–1082.